International Journal of Plasticity 131 (2020) 102730

Contents lists available at ScienceDirect

International Journal of Plasticity

journal homepage: www.elsevier.com/locate/ijplas

Microstructural characterization and constitutive modeling of deformation of closed-cell foams based on in situ x-ray tomography

H.W. Chai [a], Z.L. Xie [b], X.H. Xiao [c], H.L. Xie [d], J.Y. Huang [a,b,*], S.N. Luo [a,b,*]

[a] The Peac Institute of Multiscale Sciences, Chengdu, Sichuan 610031, PR China
[b] Key Laboratory of Advanced Technologies of Materials, Ministry of Education, and Institute of Material Dynamics, Southwest Jiaotong University, Chengdu, Sichuan 610031, PR China
[c] Advanced Photon Source, Argonne National Laboratory, Argonne, IL 60439, USA
[d] Shanghai Institute of Applied Physics, Chinese Academy of Sciences, Shanghai 201204, PR China

ARTICLE INFO

Keywords:
Polymethacrylimide foam
X-ray tomography
Deformation banding
Microstructure evolution
Constitutive modeling

ABSTRACT

Polymethacrylimide (PMI) foams own the highest specific stiffness and strength of all foams. *In situ* x-ray micro computed tomography (CT) is used to map three-dimensional (3D) microstructures of this representative closed-cell foam under quasi-static compression. The strain fields obtained via digital volume correlation reveal divergent types (discrete or spreading) of deformation banding for the PMI foam with different densities (52 or 75 kg m^{-3}). Significant cell collapse occurs in the deformation bands, leading to ~40% reduction of the mean cell size, and alignment of cell orientations. Microstructure-based finite element analysis confirms that elastic buckling of cell walls dominates cell collapse, and the buckling strength of walls depends highly on their thicknesses and inclination angles. An edge segmentation technique is then used to quantify the morphology and buckling strength index of cell walls. The spatial distribution of the weakest 3% cell walls correlates well with the modes of deformation banding. Based on elastic buckling of cell walls, new analytical models are developed to predict the strength–density scaling law and stress–strain curves of the PMI foam, which agree well with the experimental results.

1. Introduction

Cellular materials, made of metals, ceramics and polymers, etc., show excellent mechanical and biological properties (Gibson and Ashby, 1999; Kang et al., 2018; Janik and Marzec, 2015), and have been utilized in various engineering applications for energy absorption, sandwich cores, acoustic damping, thermal insulation, catalysis, and tissue repair (Kim et al., 2017; Janik and Marzec, 2015; Kang et al., 2018; Chen et al., 2019). It is now available to produce cellular materials with specific mechanical properties via tailoring porosity and cell morphology (Banhart, 2001; Bonatti and Mohr, 2017). Controlling formulation, processing and structure of cellular materials, and understanding the resultant mechanical response (especially deformation and failure) have long been of interest for fundamental and applied research (Lee et al., 2017; Bonatti and Mohr, 2017; Banda and Ghosh, 2018). However, exploring the structure–property relations at the cell scale has been an experimental challenge for real three-dimensional (3D) foams (Saadatfar et al., 2012; Sun and Li, 2018).

Extensive efforts have been devoted to characterizing bulk mechanical properties of cellular materials (including honeycombs) (Gibson and Ashby, 1999; Zaretsky et al., 2012; Chen et al., 2019; Cote et al., 2004; Wang and McDowell, 2005; Shan

* Corresponding authors at: The Peac Institute of Multiscale Sciences, Chengdu, Sichuan 610031, PR China.
E-mail addresses: jyhuang@pims.ac.cn (J.Y. Huang), sluo@pims.ac.cn (S.N. Luo).

https://doi.org/10.1016/j.ijplas.2020.102730
Received 10 September 2019; Received in revised form 14 February 2020
Available online 10 March 2020

et al., 2019). Gibson and Ashby (1999) (GA) proposed the well-known structure–property relationships for open- and closed-cell foams, i.e., the power laws which connect the Young's modulus and collapse strength of foams to those of matrix and relative density, and the exponents depend highly on cell deformation modes. However, the details of cell deformation and collapse are largely ignored when using the GA model (Kenesei et al., 2004; Wang et al., 2010) since microstructural characterizations are largely unavailable. In addition, an important structural parameter in the GA model for closed-cell foams, the fraction of solid in cell edges, is usually replaced by an empirical value (Mangipudi et al., 2016), because of the difficulty in measuring it directly. In terms of bulk stress–strain curves, the GA model (Gibson and Ashby, 1999) presents a piece-wise formulation describing three deformation stages. Based on the GA model, modeling the stress–strain curve of aluminum foams was attempted considering the effect of initial cell size distribution under the sequential-collapse assumption to be validated (Kenesei et al., 2004), but failed to reproduce the whole stress–strain curve. Many one-dimensional (1D), empirical or phenomenological constitutive models proposed for foams (Rusch, 1970; Hanssen et al., 2002; Liu and Subhash, 2004; Avalle et al., 2007; Zheng et al., 2014; Wang et al., 2018), can reproduce experimental stress–strain curves under certain circumstances, but contain empirical parameters that vary with cellular structures (e.g. initial density), and need experimental verifications. Other phenomenological models (Deshpande and Fleck, 2000; Ehlers and Markert, 2003; af Segerstad et al., 2008) considering microscopic deformation mechanisms are usually too complex to present explicit stress–strain relations, and thus not friendly for engineering applications, except aiding numerical simulations.

Deformation of foam materials under compression begins with an overall compression of the cellular structure, followed by local collapse of cells via elastic–plastic buckling of cell edges/walls (Gibson and Ashby, 1999), which gives rise to a stress plateau. During the collapse stage, deformation proceeds in localized deformation bands that nucleate and propagate within the cellular structure (Issen et al., 2005; Zaiser et al., 2013). Previous studies attempted to characterize the structural heterogeneity of foams, in terms of such quantities as local density, Minkowski anisotropic index (Saadatfar et al., 2012), cell size and cell aspect ratio (Sun et al., 2017). Recently, we proposed a single buckling strength index for cell walls incorporating their morphological parameters (Chai et al., 2019). The buckling strength index is proved effective in revealing the initial weak zones of a foam sample (Chai et al., 2019). However, the assumption that cell walls buckle elastically remains to be verified. In addition, how cell wall buckling contributes to the density–strength scaling and the stress–strain response of 3D foams is a significant but pending question (Bonatti and Mohr, 2017; Sun and Li, 2018).

Studies on microscopic deformation and failure of cells commonly resort to 2D postmortem analysis via scanning electron microscopy (Arezoo et al., 2011; Fan et al., 2018) or Voronoi-based modeling (Alkhader and Vural, 2010; Zheng et al., 2014). However, microstructures of real foams are 3D in nature; there exist distinct differences in quantification of local density, cell size and morphology of foams between 2D and 3D systems. Voronoi models also have substantial drawbacks when applied to closed-cell foams since they are unable to sufficiently capture the complexity of real cell structures (plateau borders, thickness variation and curvedness within a cell wall, etc.). Based on synchrotron x-ray sources, *in situ* micro computed tomography (CT) has been developed to characterize the evolution of 3D cellular structures (Saadatfar et al., 2012; Patterson et al., 2016; Roth et al., 2018). Micro CT can provide cell deformation details at a micron scale (Patterson et al., 2016), but quantification of microstructural changes throughout a deformation process was rarely reported, e.g. deformation bands evolution, cell collapse routes. Cell wall parameters were connected with the compressive strength of a virtual 2D foam (Sun et al., 2017), but little work has yet been done for an actual 3D foam. The thin walls of polymer foams ($< 10\,\mu m$) demand sub-micron spatial resolutions as provided by micro CT. The density effects on structural inhomogeneity and deformation modes of foams were not investigated. Recently, numerical models based on real, 3D cell structures have been developed to capture the actual meso-scale geometry (Sun et al., 2014; Naouar et al., 2015; Sun et al., 2016b; Chen et al., 2017). These studies have provided general insights into the deformation mechanisms of cellular materials. Finite element (FE) modeling with real cell structures is also adopted in this study to explore the cell-wall buckling mechanism quantitatively.

Polymethacrylimide (PMI) foams are superior to conventional foams in specific mechanical properties, and have been widely utilized in aerospace industry (Li et al., 2000; Arezoo et al., 2011; Grace et al., 2012). In the present study, quasi-static compression tests are conducted on this representative closed-cell foam, with a home-made material test system (MTS). *In situ*, micro CT is used to map the evolution of 3D microstructures of the PMI foam with two initial densities. The axial strain fields quantified via digital volume correlation (DVC) (Schrijer and Scarano, 2008; Bar-Kochba et al., 2015; Pan and Wang, 2017; van Dijk et al., 2019) reveal different deformation modes for two types of foams. Microstructure-based FE analysis confirms that cell walls buckle elastically, which leads to cell collapse. Then analytical models are developed to predict the strength–density relation and stress–strain curves of the PMI foam incorporating the microstructural evolution.

2. Experimental

2.1. Materials

Commercially available PMI foams are used as the experimental materials. Two initial foam densities, $\rho_0 = 52$ kg m^{-3} and 75 kg m^{-3}, are chosen to study the density effects on microstructures and deformation modes. The apparent initial density is measured with a $100 \times 100 \times 60$ mm^3 foam sample. The solid fraction of foams is calculated from the apparent foam density and full PMI density, i.e. 1200 kg m^{-3} (Li et al., 2000), which is 0.043 and 0.062 for the 52 kg m^{-3} and 75 kg m^{-3} foam samples, respectively. The as-received foam block is machined into cylindrical or cuboidal samples via laser cutting. The laser power is kept low to minimize damage to the cells adjacent to cutting planes.

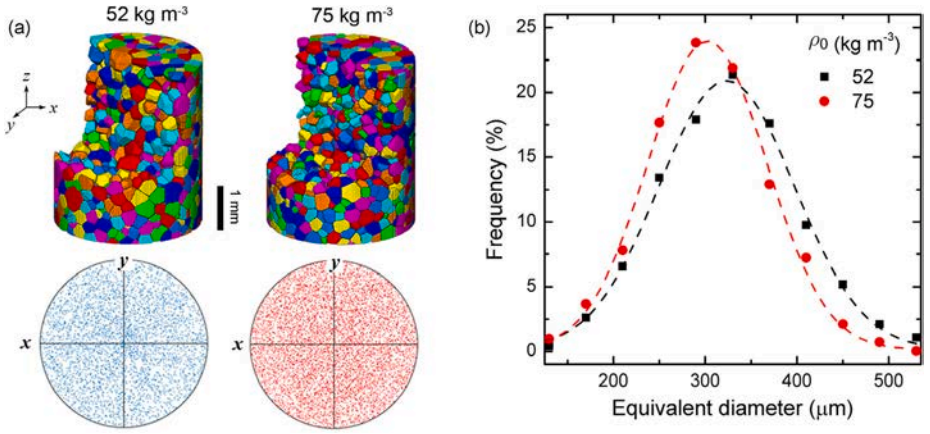

Fig. 1. CT characterizations of two as-received foams with initial density $\rho_0 = 52$ and 75 kg m^{-3}. (a) 3D renderings, and pole figures of the c-axis orientation of cells, obtained from the gyration tensor analysis. (b) Cell size (equivalent diameter) distribution. Symbols denote experimental data, and dashed lines, fitting with the Gaussian function.

2.2. Initial CT characterization

3D CT characterizations on initial foam samples are conducted in the X-ray Imaging and Biomedical Application Beamline (BL13W1) of the Shanghai Synchrotron Radiation Facility (Chen et al., 2012). The nominal resolution is chosen as 3.25 μm per pixel. Large cylindrical samples (diameter 6.5 mm, height 5.0 mm) are used to provide more statistical information on cells. The x-ray energy is set at 15 keV, and the sample-to-scintillator distance is 150 mm. The exposure time is 1 s. Each tomography scan comprise 1200 projections in 0–180°, which are then reconstructed into 3D images with a software PITRE (Chen et al., 2012). To quantify 3D foam structures, the volume images are processed in four steps: (i) an image is binarised into the solid phase and air phase via global thresholding segmentation (TS); (ii) the top-hat method (Bright and Steel, 1987) is used to recover those thin walls not extracted by TS; (iii) the fraction of solid is calculated and compared with the experimental measurements; adjust thresholds and repeat steps (i) and (ii) until the calculated and measured values are consistent (Saadatfar et al., 2012); (iv) the classic watershed is applied for cell partitioning to quantify cell morphology. The parameters are selected to minimize over-segmentation. Cell partitioning is visually inspected to repair over-segmented cells (especially at large deformations).

Characterizations of initial cell morphology in the two types of foams are presented in Fig. 1. The volume renderings (Fig. 1a) indicate that the foam cells are largely polyhedrons. Gyration tensor is introduced to characterize cell morphology (Arkın and Janke, 2013; Yao et al., 2018; Li et al., 2020),

$$G_{\alpha\beta} = \frac{1}{V_{\mathrm{m}}} \sum_{i=1}^{V_{\mathrm{m}}} \left(r_{\alpha i}^{(\mathrm{m})} - r_{\alpha}^{(\mathrm{b})} \right) \left(r_{\beta i}^{(\mathrm{m})} - r_{\beta}^{(\mathrm{b})} \right), \tag{1}$$

where $r_{\alpha i}^{(\mathrm{m})}$ and $r_{\alpha}^{(\mathrm{b})}$ ($\alpha = x, y, z$) are coordinates of voxel i, and of the barycenter (b) of cell m, respectively. V_{m} is the volume of cell m (in terms of the number of voxels enclosed by the cell walls). The eigenvalues of the gyration tensor are calculated as R_1, R_2 and R_3 ($R_1 > R_2 > R_3$). Then, a characteristic ellipsoid can be constructed with three semi-axes oriented along the eigenvectors, and their lengths $a = \sqrt{5R_1}$, $b = \sqrt{5R_2}$ and $c = \sqrt{5R_3}$. A sphericity index can be defined as $S_G = 1 - \frac{1}{2} \sum_{k,l=1(k>l)}^{3} \left(R_k - R_l \right)^2 / \left(\sum_{k=1}^{3} R_k \right)^2$, where $k, l = 1, 2, 3$.

The orientation pole figures of the c-axis for the two types of foams (Fig. 1a) show that both foams are isotropic with no preferred orientations of cells. Cell sphericity for the two types of foams is largely 0.9–1.0, indicating that the cells are close to regular polyhedrons. Cell size is defined as the equivalent sphere diameter of the pore volume enclosed by the cell. The cell size distributions of two types of foams can both be described with a Gaussian function. The mean and standard deviation of the cell size from fitting are 323 ± 1 μm and 74 ± 1 μm for the 52 kg m^{-3} foam, and 302 ± 1 μm and 65 ± 1 μm for the 75 kg m^{-3} foam, respectively.

2.3. In situ CT testing

A home-made MTS device (Fig. 2) is used for *in situ* x-ray CT under uniaxial compression at beamline 2-BM, Advanced Photon Source (Bie et al., 2017; Chai et al., 2019; Li et al., 2020). The nominal resolution is 0.87 μm per pixel, much higher than that in initial CT characterizations, and can provide deformation details of cell walls. Smaller samples of 3.5 × 3.5 × 3.7 mm are used to match the field of view, and the dimension along the loading direction (the z-axis) is 3.7 mm. The sample is sandwiched between two steel platens inside a polycarbonate (PC) tube. The upper platen is lowered to apply compression loading while the lower platen is fixed. When the preset displacement or strain level is reached, the upper platen is suspended and CT scan is carried out on the

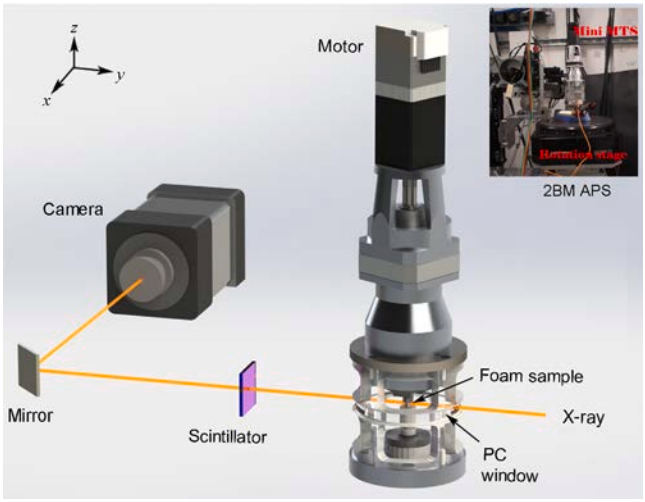

Fig. 2. Schematic diagram of *in situ* CT testing system including a miniature MTS and x-ray imaging system. Inset: photograph of the experimental setup at beamline 2-BM of APS.

deformed sample after the platen force reaches a nearly stable state (about 30 s later). Two or three scans along the sample height direction are performed to cover the whole gauge length at each deformation stage. X-rays transmitted through the PC tube and the foam sample form images on the scintillator which are captured by a camera for 3D reconstruction. The force–displacement curve measured with MTS is used to derive the axial engineering stress–strain curve.

The loading velocity is set at $0.74\ \mu m\,s^{-1}$, resulting in a nominal strain rate of $0.0002\ s^{-1}$. A previous study (Arezoo et al., 2013) showed that the rate sensitivity of the Rohacell PMI foam is minor, especially for low-density foams ($\leq 110\ kg\ m^{-3}$). Therefore, strain rate effects of the PMI foams are not discussed here.

2.4. Digital volume correlation

To study deformation dynamics of foams, an iterative DVC technique (Bar-Kochba et al., 2015) is adopted to map 3D strain fields. The gray-scale volume images are used for image correlation. To reduce computational cost, the volume images are scaled down to one tenth of its original size along each axis with the bicubic interpolation method. The region of interest (ROI) in the initial configuration is divided into proper-sized subsets, and then the subsets are tracked in the deformed configuration. The widely used correlation criterion, normalized sum of squared differences (NSSD) (Criminisi et al., 2007), is adopted here for pattern matching. NSSD eliminates effectively the influence of light and shade differences between the initial and deformed images. The NSSD correlation coefficient, C_{NSSD}, for a subset is expressed as

$$C_{\mathrm{NSSD}}(\mathbf{u}) = \frac{1}{2}\frac{\sum_{i=1}^{N}\left\{\left[I_0(\mathbf{p}_i)-\bar{I}_0\right]-\left[I_1(\mathbf{p}_i+\mathbf{u})-\bar{I}_1\right]\right\}^2}{\sum_{i=1}^{N}\left[I_0(\mathbf{p}_i)-\bar{I}_0\right]^2+\sum_{i=1}^{N}\left[I_1(\mathbf{p}_i+\mathbf{u})-\bar{I}_1\right]^2}, \tag{2}$$

where $I_0(\mathbf{p}_i)$ and $I_1(\mathbf{p}_i+\mathbf{u})$ refer to the intensity values of a voxel i located at $\mathbf{p}_i = (x_i, y_i, z_i)$ in the subsets before and after deformation, respectively. $\mathbf{u}$ is the displacement vector of the subset. $\bar{I}_0$ and $\bar{I}_1$ are the mean intensities of the subset before and after deformation, respectively. $N = N_x N_y N_z$ is the total number of voxels in the subset, where N_x, N_y and N_z are the subset size in the x-, y- and z-directions, respectively. C_{NSSD} ranges from 0 to 1, and a larger C_{NSSD} indicates lower correlation. The displacement calculation in the subsets with C_{NSSD} greater than a threshold $C_{\mathrm{NSSD}}^{\mathrm{th}}$ is deemed invalid and set to zero.

In iterative DVC, multiple cycles of tracking and correlation are conducted to gain high accuracy of deformation calculation. In a specific cycle, the program flow is as follows. First of all, the displacement vector yielding the minimum C_{NSSD} is identified as the incremental displacement in the current cycle. The total displacement of the subset is the summation of the previous displacement and the incremental one. The 3D displacement field is obtained via interpolation from all voxels. After that, a low-pass convolution filter (Schrijer and Scarano, 2008) is used to smooth the field. The filter strength controls the smooth degree and shows the optimal dampening and modulation characteristics over the range of 0.001–0.01 (Schrijer and Scarano, 2008). Finally, the initial and deformed images are warped (via trilinear interpolation) symmetrically by the current displacement field (Bar-Kochba et al., 2015). If the warped initial and deformed images reach the same configuration, iteration is stopped and the final displacement field is obtained. Otherwise, iterative correlation, filter and warping are carried out on the warped images from the current cycle. The subset size for the following cycle is reduced by half and remains constant when it reaches a lower limit. The corresponding strain fields are evaluated by calculating the Lagrangian strain tensor.

$$\varepsilon_{ij} = \frac{1}{2}\left(\frac{\partial u_i}{\partial x_j}+\frac{\partial u_j}{\partial x_i}+\frac{\partial u_m}{\partial x_i}\frac{\partial u_m}{\partial x_j}\right), \tag{3}$$

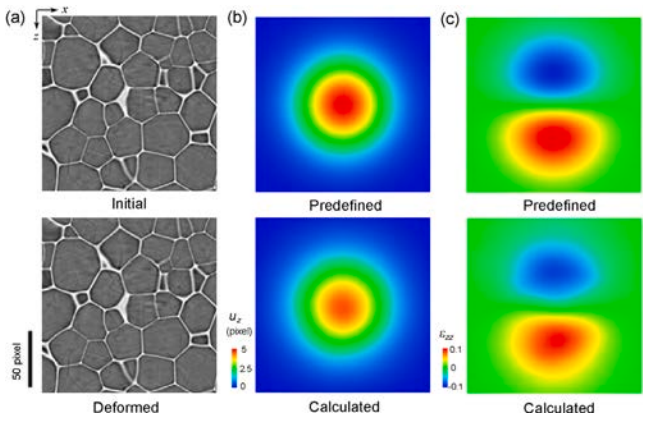

Fig. 3. Error analyses for DVC. (a) Gray-scale xz slices of foams before (initial) and after (deformed) virtual 3D Gaussian deformation in the loading or z direction. (b) and (c) Comparison of the xz contour plot of the predefined and calculated displacement and strain ε_{zz} fields.

Table 1
Parameters and precision for DVC analyses.

Parameter	Value
Initial subset size (pixel)	(32, 32, 64)
Minimum subset size (pixel)	(32, 32, 32)
$C^{\text{th}}_{\text{NSSD}}$	0.5
Filter strength	0.075
Displacement precision (pixel)	0.08
Strain precision (%)	0.41

where $1 \le i, j, m \le 3$ (1, 2 and 3 corresponding to x, y and z, respectively), and the Einstein summation convention is applied. The central difference method is used to calculate the partial differential or gradient of the displacement field. For boundary voxels, a single-sided difference method is adopted instead of the central difference method.

The subset size plays an important role in the calculation accuracy of DVC. Since iterative correlation is adopted, the lower limit for subset size or minimum subset size has higher influence on DVC analysis than initial subset size. The minimum subset size is identified according to the cellular structure. The diameters of most cells (Fig. 1(b)) in the two types of foams are smaller than 500 μm (56 pixels for scaled images). Assume that a half cell contains sufficient features for track. Then the subset size is supposed to exceed 28 pixels. The program flow requires that the subset size be the power of 2. Therefore, $(N_x, N_y, N_z) = (32, 32, 32)$ is set as the minimum subset size while (32, 32, 64) as the initial one. N_z is larger in the initial subset since deformation is mainly along the z-direction in the experiments. The parameters used in DVC analyses are summarized in Table 1.

To evaluate the performance of DVC, a virtual displacement field is imposed to the gray-scale images (Fig. 3a) in two steps (van Dijk et al., 2019). Firstly, the current coordinates of the centers of all reference (undeformed) voxels are calculated based on a 3D Gaussian displacement field $\mathbf{u} = (0, 0, u_z)$; $u_z(x, y, z) = 5\exp\left[-(x^2 + y^2 + z^2)/(2 \times 30^2)\right]$ pixel, where x, y, z are the coordinates of voxels. Secondly, the gray-scale values are calculated for the regularly spaced centers of all current (deformed) voxels by linear interpolation. This linear interpolation is based on an unstructured set of data points, and the standard Delaunay triangulation is used. $C^{\text{th}}_{\text{NSSD}}$ is set as 0.5 to minimize invalid correlation. The calculated displacement field via DVC is presented in Fig. 3b, and agrees well with the preset displacement field. The calculated and preset displacement fields are then used to derive the strain component ε_{zz}, and the strain maps are presented in Fig. 3c. The calculated strain field coincides with the preset one, and can reproduce well the strain localization features, which is critical for identifying deformation bands in the foam samples. A common and efficient measure for comparing results is the precision (van Dijk et al., 2019), defined as the standard deviation of the error distribution $e(x, y, z)$. $e(x, y, z)$ is obtained by comparing the calculated results and the exact solution. The precision for displacement calculation is 0.08 pixel and for ε_{zz} strain calculation is 0.41%, sufficient for strain mapping in foam materials.

3. Experimental results

3.1. In situ CT analysis

The axial engineering stress–strain curves of the two types of foam samples along with the volume renderings at different strains are presented in Fig. 4. Here, positive stress refers to compression, and positive strain, to contraction. The solid curves with stress drops are from *in situ* CT test with pauses, consistent with the dashed curves from continuous loading. The continuous stress–strain curve is averaged from five repeated tests. The stress–strain curve can be divided into three stages, i.e. pre-collapse, collapse and densification. Here "pre-collapse" is used instead of "elastic" (Wang et al., 2018) because plastic deformation can occur in cells at

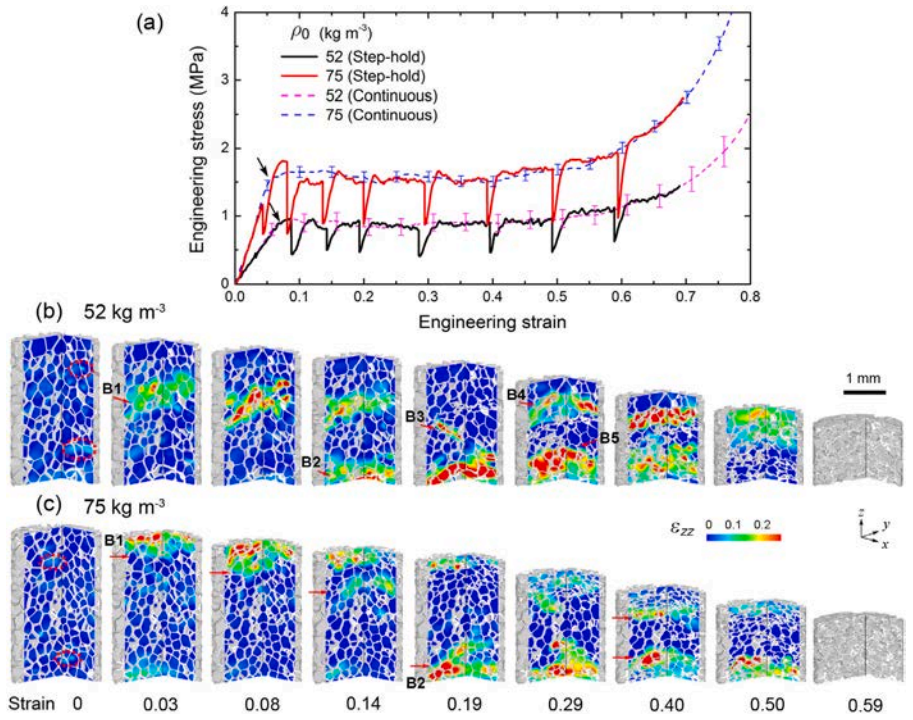

Fig. 4. *In situ* CT testing of the two types of foams (ρ_0 = 52 and 75 kg m^{-3}). (a) Stress–strain curves. The solid curves with stress drops are from *in situ* CT test with pauses (step-hold), while the dashed curves are from continuous loading. (b) and (c) Volume renderings at different axial strains for the 52 kg m^{-3} and the 75 kg m^{-3} foam samples, respectively. Color-coding refers to axial strain fields (ε_{zz}) obtained via DVC. Positive strain refers to contraction.

this stage (Sun et al., 2016a, 2014). The Young's modulus and collapse strength increase while the initiation strain of densification decreases with increasing initial foam density (Fig. 4a). The collapse strength of the foam is taken as the stress at the inflection point (indicated by arrows) between the pre-collapse and collapse stage.

Axial strain fields ($\varepsilon_{zz}(x, y, z)$) across the foam sample throughout its deformation process are obtained via the DVC technique. Fig. 4b and c show strain maps on the xy and xz slices for the 52 kg m^{-3} and 75 kg m^{-3} foam samples, respectively. Correlation is carried out between tomographs at two adjacent strain levels and the strain field is mapped on the previous tomograph. The strain fields show three stages of deformation, consistent with the stress–strain curve. At the pre-collapse stage (e.g. 3%), the foam samples deform via an overall compression of the cell skeleton accompanied by slight bending or buckling of some "weak" walls, resulting in a nearly uniform strain field with low magnitudes. Local buckling of these walls leads to some higher-than-average strain values (marked by dashed circles). During the collapse stage, deformation banding occurs in both types of foam samples, as shown in strain maps at 8%–50%. Pronounced strain localization (about 5 times the average strain across the sample) and cell wall buckling are detected within these bands. After about 60% strain, deformation bands coalesce, and the incremental strain becomes minor across the sample, resulting in the macroscopic densification of the foam samples.

Deformation modes are different for the two types of foam samples. Multiple, discrete deformation bands are formed sequentially in the 52 kg m^{-3} sample (marked as B1–B5, Fig. 4b), while spreading bands initiated at the ends of the 75 kg m^{-3} sample develop alternately and propagate gradually across the sample (marked by arrows in Fig. 4c). The thickness of a single deformation band, calculated as the full width at half maximum of the strain profiles, is 300–500 μm, spanning across 1–2 cell layers. The propagation velocity of the upper deformation front is estimated (from strain maps at 8%–19% strain, Fig. 4c) as 0.74 μm s^{-1}. In addition to *in situ* CT test, a total of ten compression tests are conducted with *in situ* optical imaging to examine the repeatability of the deformation modes. For most (~80%) of the 75 kg m^{-3} samples, deformation bands are initiated at one or two sample ends and spread toward sample center, while the majority of the 52 kg m^{-3} samples (~70%) show discrete deformation bands.

3.2. Cell deformation and failure

Cell partitioning (Section 2.2) is applied to binarised volume data at different strains to separate deformed cells. During cell collapse, cell walls buckle and two initially separated walls come into contact with each other. Some fully contacted walls split the original cell into two or more disconnected spaces which are defined as new cells. Counting the number of cells in each volume data indicates a slight increase in the cell number when the axial strain exceeds about 40%. We remove cells whose equivalent diameter is smaller than 25 μm to reduce the noise.

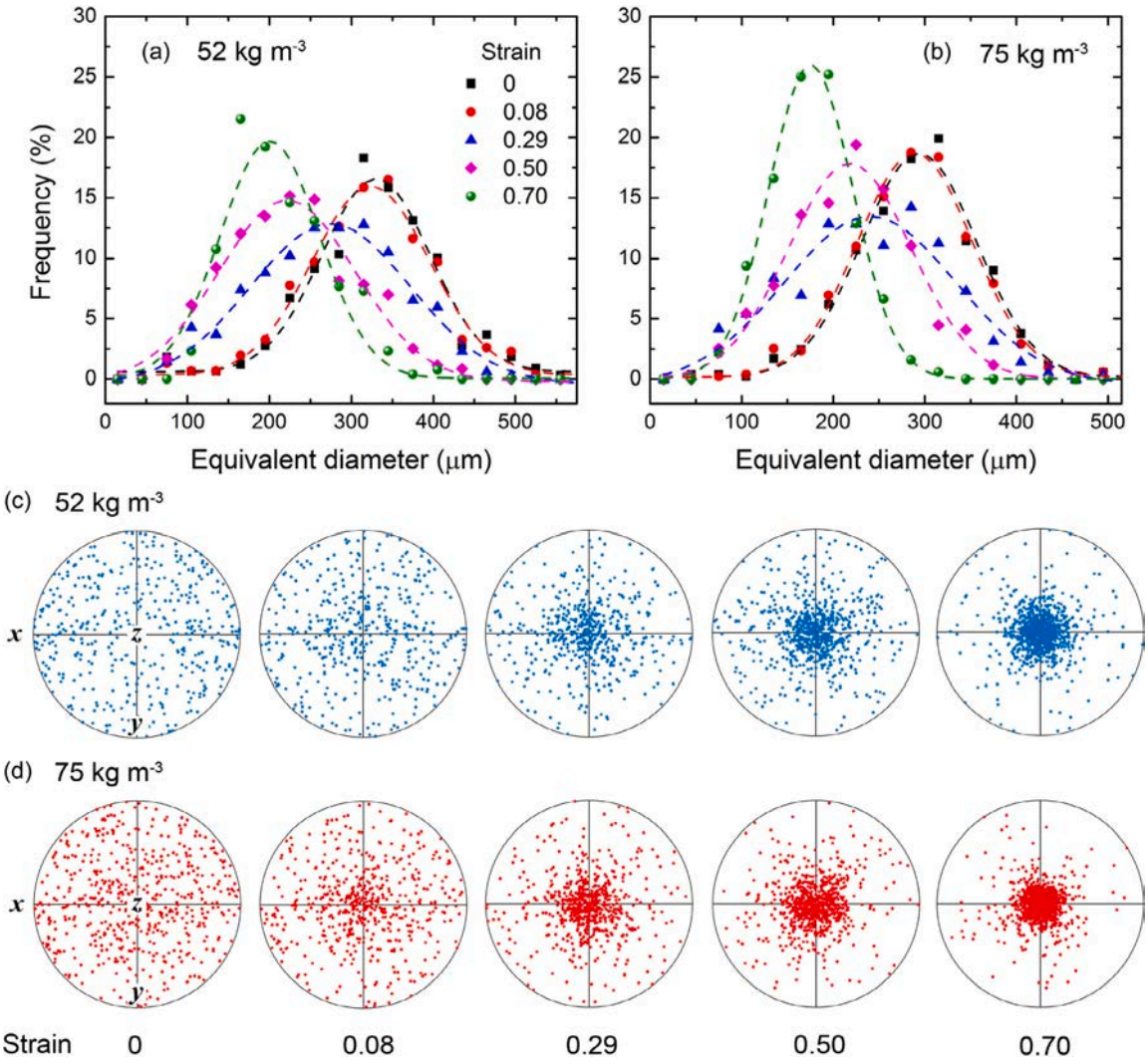

Fig. 5. Microstructural evolution of the two types of foams at different axial strains. (a) and (b) Cell size distributions. Symbols refer to experimental data, and dashed lines, fitting with the Gaussian function. (c) and (d) Pole figures of the *c*-axis orientation of cells.

Fig. 5a and b show the evolution of cell size distributions for the two types of foams. Curves at only five representative strains are given for clarity. The dashed lines are Gaussian fitting to the experimental data. The cell size distributions conform to the Gaussian function throughout the deformation process. They remain approximately unchanged when the axial strain is smaller than 8%. After that, their peaks shift toward smaller cells as deformation progresses. The mean cell size decreases by about 40% at 70% strain for both types of foams. The distributions become broadened due to localized cell collapse, and then narrowed after about 50% strain. Cell collapse leads to considerable shrinkage of cell volume, and consequently the observed peak shift and shape change in the cell size distributions. However, the cells are not totally compacted in the densification stage, and a certain amount of voids are arrested in the collapsed cells. Evolution of the orientation of the cell *c*-axis for the two types of foams is presented in Fig. 5c and d. The cells are randomly oriented initially, consistent with the results for larger samples (Fig. 1b). When the axial strain exceeds 8%, the *c*-axis orientations of cells converge gradually to the loading direction (*z* axis) as deformation progresses, leading to increasing anisotropy in the sample. The reason is that most cells after collapse become flat with their normals (the *c*-axis) oriented along the loading direction, regardless of their initial orientations. These microstructural changes provide first-hand information or verificaton for phenomenological constitutive models and numerical modeling.

To clarify how cells collapse, we track the deformation and collapse of four typical cells (A–D, Fig. 6a–d) in the 75 kg m^{-3} sample. As shown in Fig. 6e, cells A, B and C are in the same cell layer (0.8 mm away from the sample top), but with different shapes. The position of cell D is about 0.9 mm lower than that of cell A, but cell D is similar in size and shape to cell A. Cells A and D have higher sphericity than cells B and C which are elongated along the *x* and *z* direction, respectively. A curvature index *C* proposed by Koenderink and Van Doorn (1992) is mapped on the cell surfaces to highlight the wrinkles of cell walls, which is

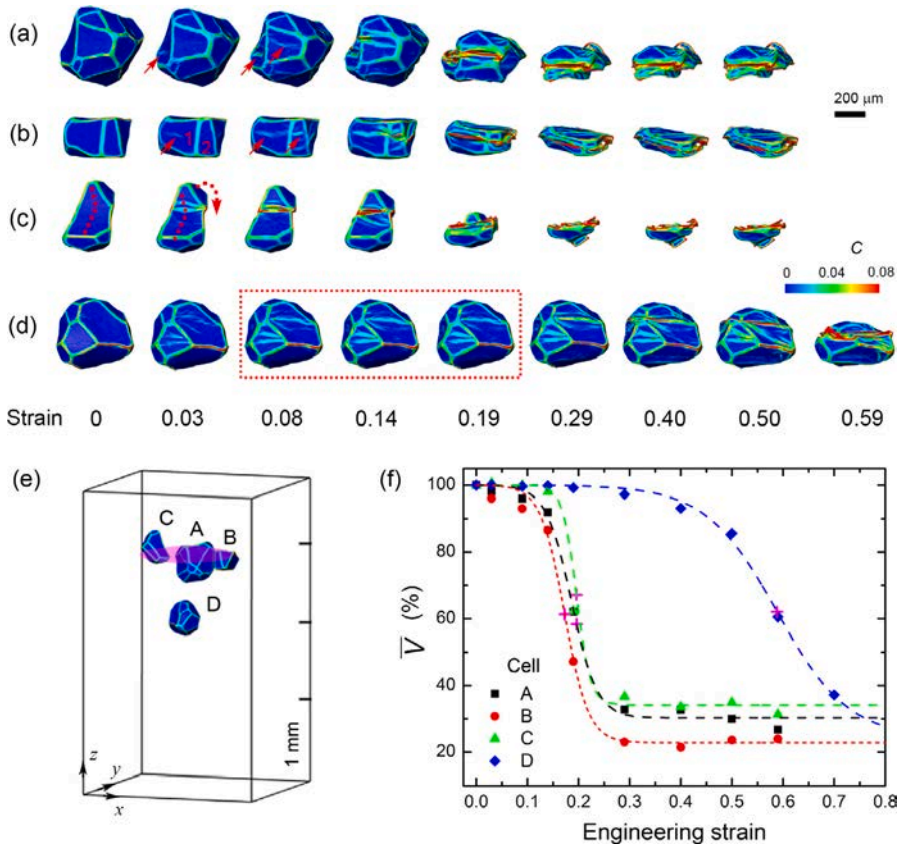

Fig. 6. Deformation and collapse of four typical cells A–D in the 75 kg m^{-3} foam sample at different strains. (a)–(d) correspond to cells A–D, respectively. Color-coding is based on curvature index, C, which highlights buckling of cell walls (wrinkles). (e) Initial positions of four cells in the sample. (f) Normalized cell volume $\overline{V}$ as a function of axial strain for the four cells. Symbols denote experimental measurements, and dashed lines, fitting with the Boltzmann sigmoid function.

defined as

$$C = \sqrt{\frac{\kappa_1^2 + \kappa_2^2}{2}}, \tag{4}$$

where κ_1 and κ_2 are two principal curvatures of a point on a cell surface.

The curvature is around zero across all cell walls at the initial state. At 3% strain, wrinkles initiate on one of the walls for cells A–D (marked by arrows), while edges remain intact. With increasing loading, the nucleated wrinkles grow and new wrinkles form on other walls. Cells A–C collapse abruptly at 19% strain, when the deformation band initiated at the upper end of sample propagates into this layer (see the strain map at 14% strain, Fig. 4c). Cell D has a similar size and shape to those of cell A, but collapses at a much later time. The wrinkles in cell D stay stable after 8% strain (marked by the dashed rectangle), and then regrow at 29% strain, leading to cell collapse at around 50% strain when the upper deformation front arrives. Therefore, cell deformation and collapse are highly affected by their locations and shapes. Similar results are observed in the 52 kg m^{-3} sample.

Cell collapse in the PMI foam initiates via local *cell wall buckling*, and different walls show different resistance to buckling. For cell B, wrinkles initiate earlier in a wide wall (numbered 1) than in an adjacent narrow one (numbered 2). The wider wall seems more prone to buckle. However, obvious wrinkles are observed on a slender wall of cell C, which is expected to be buckling resistant since the width of this wall is small. The reason is that this wall is initially curved, as marked by the dashed line. The wrinkles are a result of compression-induced bending (marked by the arrow) rather than buckling. Since the cell walls are largely flat, this bending mode in the PMI foam is not dominant.

Evolution of the normalized cell volume $\overline{V}$ with the axial strain ε for four cells A–D is presented in Fig. 6f. Here $\overline{V} = V/V_0$, and V and V_0 are the current and initial volume of a cell, respectively. $\overline{V}(\varepsilon)$ can be described with a Boltzmann sigmoid function,

$$\overline{V}(\varepsilon) = A_2 + \frac{A_1 - A_2}{1 + \exp\left(\frac{\varepsilon - \zeta}{\eta}\right)}, \tag{5}$$

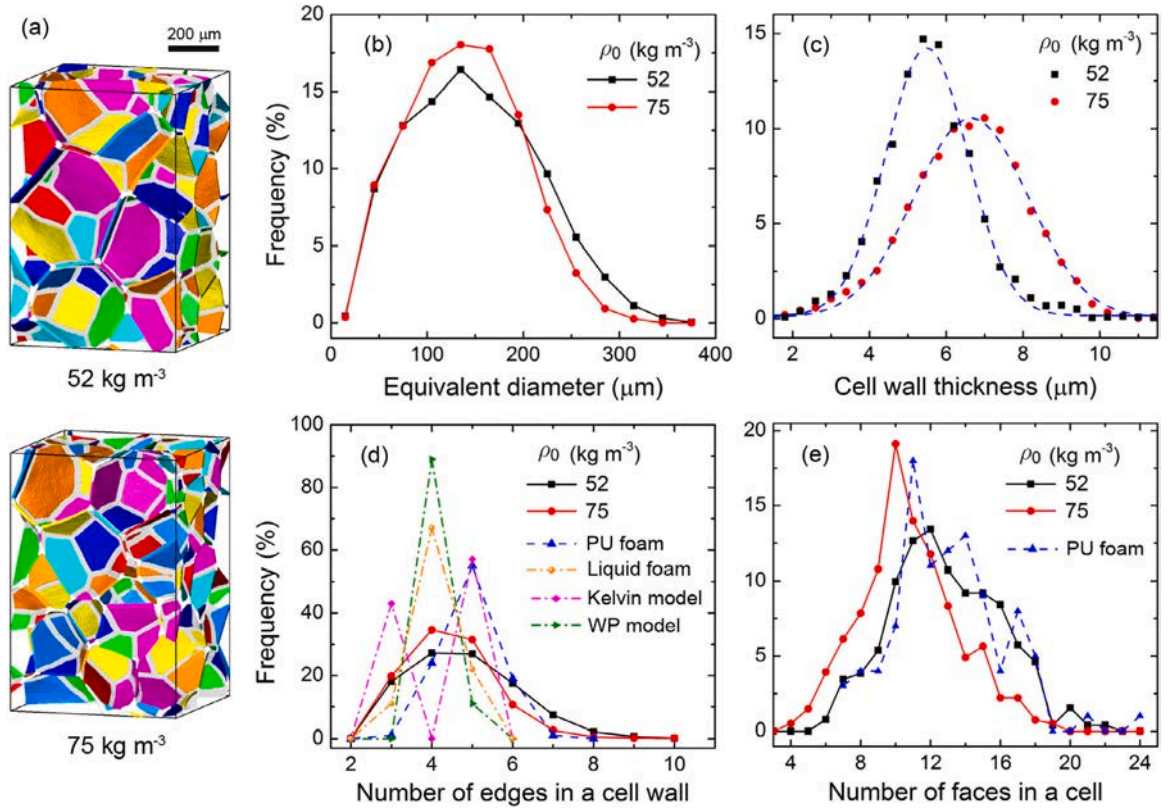

Fig. 7. Characterizations of cell wall morphology in the two types of foam samples (ρ_0 = 52 kg m^{-3} and 75 kg m^{-3}). (a) Volume rendering after edge segmentation. (b) Equivalent diameter distribution of cell walls. (c) Cell wall thickness distributions. Symbols refer to experimental data, and dashed lines, fitting with the Gaussian function. (d) Edge number distribution of cell walls. Experimental measurements for a PU foam (Montminy et al., 2004) and liquid foams (Matzke, 1946), and theoretical predictions from the Kelvin model and Weaire–Phelan (WP) model (Weaire and Phelan, 1994) are also presented for comparison. (e) Face number distribution of cells. Experimental measurements for a PU foam (Montminy et al., 2004) is presented for comparison.

where $A_1 = 1$ and A_2 are the initial and final values of $\overline{V}$; ζ is the strain at the curve center (marked by "+") and is defined as the collapse moment; η is the slope or "rate" of change in $\overline{V}$, and describes the steepness of the curve, with a larger value denoting a shallower curve. Cells A, B and C collapse at similar strains (ζ = 18.6%±0.3%, 17.3%±0.3% and 19.6%±0.1%) and rates (η = 2.5%±0.4%, 2.3%±0.3% and 1.4%±0.1%), while cell D collapses at a much higher strain (ζ = 58.8%±1.3%) and a lower rate (η = 7.0%±0.7%). The residual normalized volume A_2 is 30.2%±1.1%, 22.8%±1.4%, 34.1%±0.01% and 24.3%±5.2% for the four cells, respectively. The collapse moment of cells is consistent with the time when the deformation bands pass by them, indicating that local cell collapse leads to deformation banding there. Cells with wrinkled walls (like D) are actually in a metastable state, before triggered by deformation banding in a neighboring layer.

3.3. Cell wall morphology

Since buckling of cell walls dominates cell collapse, 3D characterizations of cell wall morphology are conducted for the two types of foams (Fig. 7). The edge segmentation technique (Chai et al., 2019) is used to separate edges and walls, mainly based on three steps: (i) edge core detection on slices by the 2D Harris operator (Harris and Stephens, 1988); (ii) estimating the edge thickness distribution from slices using the distance transform method (Sun et al., 2017); (iii) local segmentation of edge and wall voxels with a global threshold, determined as the edge thickness corresponding to a 90% cumulative probability in the edge thickness distribution. The optimum threshold is chosen iteratively as 9.0 pixels and 12.5 pixels for the 52 kg m^{-3} and 75 kg m^{-3} foams, respectively. The separated walls and edge skeletons are illustrated in Fig. 7a. The geometric parameters of cell walls can be extracted and analyzed, as illustrated in Fig. 7b–e. Cell wall size is defined as the equivalent diameter of wall projections along the thickness direction. Cell wall thickness is calculated as its volume divided by the projection area. The figures show that the 52 kg m^{-3} foam exhibits a much wider distribution of cell wall size and shapes, which introduces higher *diversity* into 3D structures.

Compared to the 52 kg m^{-3} foam, the 75 kg m^{-3} foam has smaller cell walls on average (152 μm versus 142 μm), and a narrower distribution of cell wall size (Fig. 7b), consistent with the cell size distribution (Fig. 1b). The cell wall thickness distributions of the two types of foam samples follow a Gaussian distribution (Fig. 7c). The mean and standard deviation of the wall thickness from fitting are 5.49±0.02 μm and 1.06±0.02 μm for the 52 kg m^{-3} foam, slightly lower than those (6.65±0.02 μm and 1.48±0.02 μm) of the

Table 2
Parameters in FE modeling of the PMI foam.

Bulk density of full-density PMI (kg m^{-3})	1200
Young's modulus of full-density PMI (MPa)	5200
Poisson's ratio of full-density PMI	0.4
Yield strength of full-density PMI (MPa)	90
Friction coefficient between plate and sample	0.2
Loading velocity of plate (μm s^{-1})	8.7

75 kg m^{-3} foam. The mean wall thickness here is comparable to those reported for the Rohacell PMI foam of the same density (Li et al., 2000; Arezoo et al., 2011). Fig. 7d shows that the cell-wall shapes of PMI foams vary widely from triangles to heptagons, with the majority as quadrilaterals and pentagons. There are few polygons with eight or more edges in both types of foams. The PMI foam has a much more diverse cell-wall shape distribution than those measured from a 34 kg m^{-3} PU foam (Montminy et al., 2004) and liquid foams (Matzke, 1946), and hypothesized in area minimizing models, e.g. Kelvin model and Weaire–Phelan (WP) model (Weaire and Phelan, 1994). This highlights the facts that the topological structures of polymeric foams do not follow those of ideal theoretical structures. The face number per cell also varies widely from 6 to 16 in the two types of foams (Fig. 7e). The cell shape distribution of the 52 kg m^{-3} PMI foam is much wider than that of the 75 kg m^{-3} foam, and is similar to that of the 34 kg m^{-3} PU foam (Montminy et al., 2004).

Since the edges and walls are separated, the initial fraction of solid in edges, ϕ_0, can be calculated accurately. The results are 24.5% and 39.0% for the 52 kg m^{-3} and 75 kg m^{-3} foam samples, respectively. ϕ_0 of the PMI foam is much smaller than conventional polymer foams with similar densities, e.g., $\phi_0 \simeq 0.8$ for an 80 kg m^{-3} rigid polyurethane (PU) foam (Gibson and Ashby, 1999). The reason is that cell walls in the PMI foam are flat, and similar in thickness to edges. However, the PU foams generally have spherical cells with thin curved walls, resulting in a large plateau border and high ϕ_0.

4. Finite element modeling

3D FE modeling with real PMI foam structures is used here to address the following question: whether cell walls are subjected to elastic buckling during cell collapse. The initial structures of the foam sample are used as the starting configuration for FE analysis. The 75 kg m^{-3} sample is chosen for the illustrative purpose. Since the cell walls are thin, mesh size should be sufficiently small (~2 μm here) to guarantee at least two mesh layers across the wall thickness, and the resultant mesh number is prohibitively large for the whole configuration. In order to reduce computational cost, a volume of $0.52 \times 0.52 \times 0.52$ mm^3 is randomly cropped from the middle part of the binarized volume data, and then converted into a surface mesh with triangular elements. The surface mesh is refined with interaction, aspect ratio, and holes considered, and finally converted into a volume mesh. The meshed volume has a total of 2,865,263 elements (Fig. 8a). The modified quadric tetrahedron element (C3D10M) is used to improve stress accuracy (Chen et al., 2017).

The volume mesh configuration is then imported into commercial code Abaqus/Explicit, along with material properties of the full-density PMI (Li et al., 2000), and boundary and loading conditions for FE analysis. An elastic-perfectly-plastic model is applied to the full-density PMI, and the relevant parameters listed in Table 2. In reality, movement of the sides of the cropped volume are restricted by the foam surrounding it. Therefore, six dummy plates are placed on each free face of the foam sample (Patterson et al., 2016), thereby preventing the foam from expanding in any direction (i.e. zero Poisson's ratio). Six degrees of freedom of all the plates are constrained, except the top/bottom plates which are allowed to move downward/upward along the z-axis or compressing direction. The loading velocity is set at 8.7 μm s^{-1}, resulting in a strain rate of 0.03 s^{-1}.

The axial stress–strain curve along with snapshots of the numerical and experimental samples at different axial strain levels (marked by squares) is shown in Fig. 8b–d. The collapse strength of the numerical sample is 0.57 MPa, much lower than the experimental measurement, because the numerical configuration for FE analysis contains only three cell layers, and such a reduced size leads to lower stresses (Bastawros et al., 2000). An xz section is chosen to show the structural evolution of inner cell walls, labeled 1–7 for convenience. The equivalent plastic strain ε_q^p (Safaei et al., 2014) is mapped on cells (Fig. 8c) to monitor plasticity initiation in them.

Cell walls are compressed elastically ($\varepsilon_q^p = 0$) and exhibit no curvature at very small axial strains ($\varepsilon < 0.6\%$). With increasing loading, the cell walls with small thicknesses and/or high inclination angles (e.g. walls 2 and 4) buckle first, leading to slight inflection in the stress–strain curve (marked by the arrow, Fig. 8(b)). Wavy wrinkles form in these walls (marked by arrows in the snapshot at 1.3% strain, Fig. 8c), consistent with the experimental configuration at 3% strain (Fig. 8d) where walls 2 and 4 also buckle in the pre-collapse stage. ε_q^p remains zero in walls 2 and 4, indicating that they buckle elastically. Under further compression, the buckling displacements of walls increase, plastic deformation occurs in the wrinkles, and cell walls with larger thicknesses and lower inclination angles start to buckle, resulting in a plateau in the stress–strain curve. For instance, walls 7 and 1 are observed to buckle at 2.1% and 2.6% strain, respectively, both with negligible plastic strain across the walls. Buckling of walls 1 and 7 also occurs in a similar way in the experimental sample, as illustrated in the snapshot at 8% strain. However, the experimental buckling displacements are much smaller than those in the numerical sample, because the axial strain is largely localized at the sample ends in the experiment. Remarkable plastic deformation accumulates in the wrinkled cell walls at 8% strain. Nonetheless, the walls nearly perpendicular to the loading direction (e.g. walls 3 and 6) remain intact even at high axial strains (e.g. 11%). Therefore, the buckling resistance of cell walls is highly dependent on their thicknesses and inclination angles, which will be quantitatively discussed in Section 5.1.

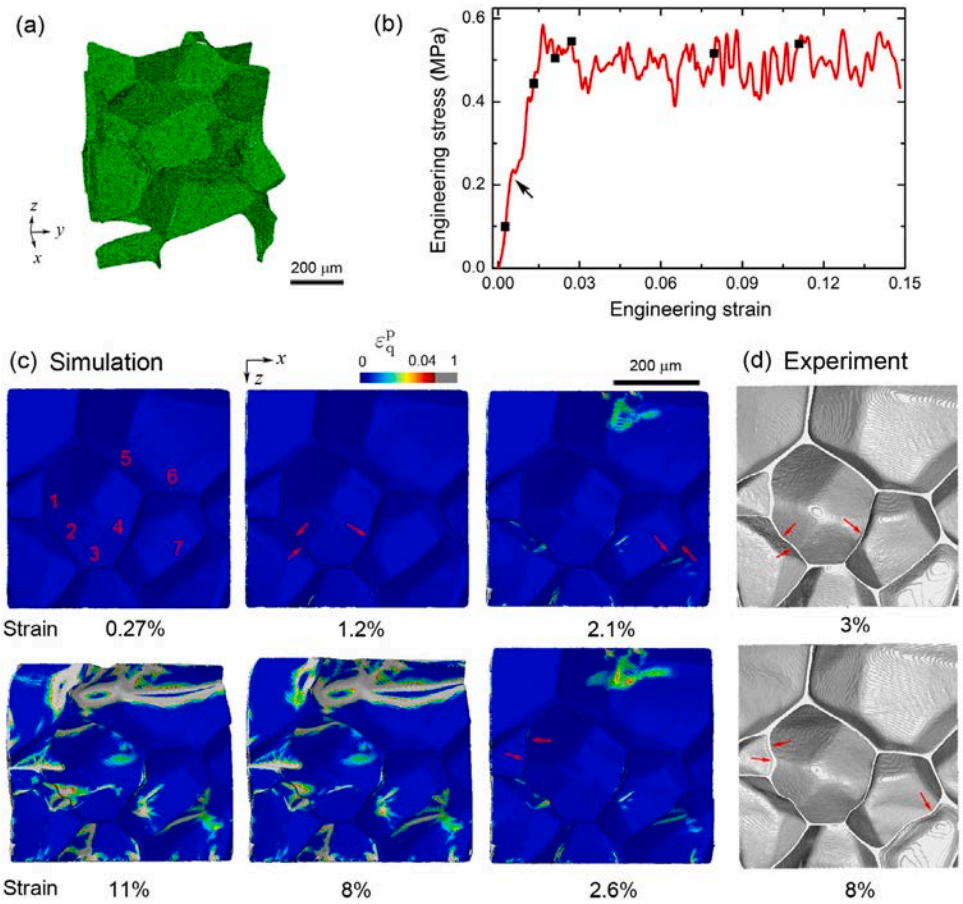

Fig. 8. FE modeling of the foam with an initial density of 75 kg m^{-3}. (a) CT-derived 3D model of the initial foam. (b) Axial stress–strain curve. (c) Snapshots of the numerical foam sample at different strains corresponding to the squares on the stress–strain curve. The equivalent plastic strain ε_q^p is mapped on cells. (d) Snapshots of the experimental foam sample at two axial strains.

Table 3
Structural and mechanical parameters of two types of PMI foam samples. For structural parameters, mean values are given along with standard deviations in parentheses. ρ_0: initial density; d_c: cell size, defined as the equivalent sphere diameter; S_G: sphericity; N_w: number of walls per cell; d_w: cell wall size, defined as the equivalent circle diameter; t_w: wall thickness; N_s: number of edges per wall; σ_c: collapse strength; ε_c: collapse strain.

ρ_0 (kg m^{-3})	Cell parameters			Cell wall parameters			Mechanical parameters	
	d_c (μm)	S_G	N_w	d_w (μm)	t_w (μm)	N_s	σ_c (MPa)	ε_c
52	323 (74)	0.95 (0.04)	11.4 (3.4)	152 (67)	5.49 (1.06)	4.8 (1.3)	1.48 (0.13)	0.066 (0.007)
75	302 (65)	0.94 (0.04)	9.2 (2.7)	142 (48)	6.65 (1.48)	4.4 (1.1)	0.87 (0.13)	0.057 (0.004)

5. Discussions

Before elaborating discussions on the experimental results, the morphological parameters of cells and cell walls and the mechanical parameters of the foam sample for the two types of foams are summarized in Table 3. The initial density shows significant influence on the microstructures and thus bulk mechanical properties of the PMI foams.

5.1. Prediction of deformation bands

Prediction of the location and moment for deformation band nucleation is critical for understanding macroscopic responses of cellular materials. The experimental and numerical results suggest that elastic buckling of cell walls determines cell collapse and thus deformation band nucleation. To quantify the the buckling resistance of cell walls, a strength index λ_w has been proposed by Chai et al. (2019) based on the elastic buckling theory of thin plates (Timoshenko and James, 1961).

$$\lambda_w = K(h_w, b_w)\frac{t_w^2}{b_w^2}\frac{1}{\sin\beta}, \tag{6}$$

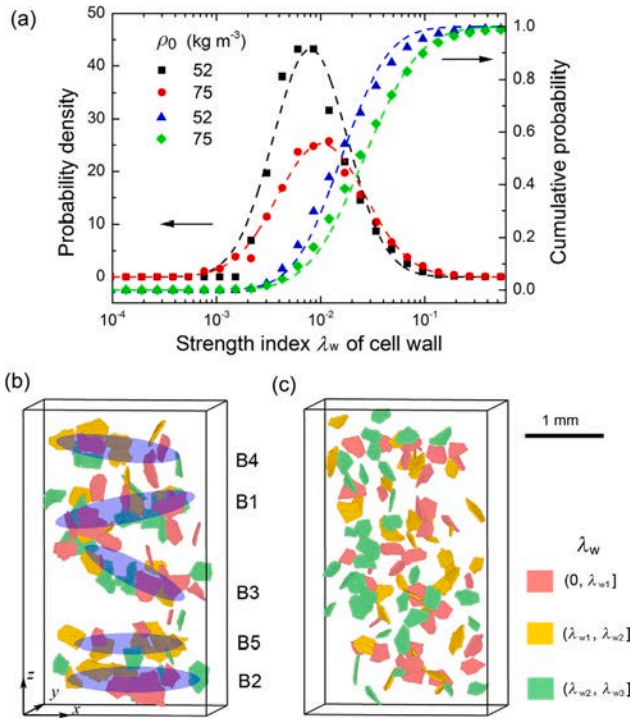

Fig. 9. (a) Probability distribution of strength index of cell walls. Symbols denote experimental data, and dashed lines, fitting with the lognormal (probability dnsity and cumulative distribution) function. (b) Spatial distribution of strength index along the sample height direction. λ_{w1}, λ_{w2} and λ_{w3} are thresholds corresponding to a cumulative probability of 1%, 2% and 3%, respectively. For ρ_0 = 52 kg m^{-3}, λ_{w1} = 0.0028, λ_{w2} = 0.0033 and λ_{w3} = 0.0037; for ρ_0 = 75 kg m^{-3}, λ_{w1} = 0.0029, λ_{w2} = 0.0038 and λ_{w3} = 0.0044. (For interpretation of the references to color in this figure legend, the reader is referred to the web version of this article.)

where $K(h_w, b_w)$ is the elastic buckling coefficient. $K = (b_w/h_w + h_w/b_w)^2$ for $h_w/b_w \le \sqrt{2}$, and $K = 4$ for $h_w/b_w > \sqrt{2}$. t_w, h_w, b_w and β are the thickness, equivalent height, equivalent width and inclination angle of a cell wall, respectively. For clarity, a local coordinate system $Ox^*y^*z^*$ is created on the center plane of the wall, where the x^*-axis is parallel to the projection of the loading direction on the wall, the z^*-axis is oriented along the wall normal, and O is set at the barycenter. h_w and b_w are defined as

$$h_w = \frac{1}{x^*_{max} - x^*_{min}} \int_{x^*_{min}}^{x^*_{max}} h(x^*)\mathrm{d}x^*,$$
$$b_w = \frac{1}{y^*_{max} - y^*_{min}} \int_{y^*_{min}}^{y^*_{max}} b(y^*)\mathrm{d}y^*, \tag{7}$$

where $h(x^*)$ is the intersection line between the y^*z^*-plane and wall; $b(y^*)$ is the intersection line between the x^*z^*-plane and wall.

The buckling strength for cell walls of two types of foams are calculated and the probability distributions are presented in Fig. 9a. The strength factor exhibits a lognormal distribution (dashed curves), and the probability density function (PDF) is

$$P(\lambda_w) = \frac{1}{\pi\omega\lambda_w} \exp\left[-\frac{(\ln\lambda_w - \mu)^2}{2\omega^2}\right], \tag{8}$$

where μ and ω are, respectively, the mean and standard deviation of the natural logarithm of λ_w. The parameters from fitting are $\mu = -4.15 \pm 0.03$ and $\omega = 0.83 \pm 0.02$ for the 52 kg m^{-3} foam, and are $\mu = -3.65 \pm 0.02$ and $\omega = 0.97 \pm 0.01$. The cell walls of the 75 kg m^{-3} foam are statistically stronger than those of the 52 kg m^{-3} foam, giving rise to a higher collapse strength.

Under quasi-static loading, damage nucleation can occur anywhere at the weakest link of sample. Therefore, we study the spatial distribution of the weakest 3% cell walls sorted by λ_w (Fig. 9b and c). Color-coding (red, yellow and green) refers to three regimes of buckling strength index, i.e., $(0, \lambda_{w1}]$, $(\lambda_{w1}, \lambda_{w2}]$, and $(\lambda_{w2}, \lambda_{w3}]$, respectively. Here, λ_{w1}, λ_{w2} and λ_{w3} are thresholds corresponding to a cumulative probability of 1%, 2% and 3% (Fig. 9a), respectively. The weakest 3% ($\lambda_w \le \lambda_{w3}$) walls in the 52 kg m^{-3} foam are located approximately at five positions where the five deformation bands nucleate in the experiment (B1–B5, Fig. 4b). The region with the highest density of flexible walls consists with the first nucleated band B1. However, the weakest 3% walls are more uniformly distributed across the 75 kg m^{-3} foam sample. There are no obvious concentration of weak walls and thus preferential nucleation sites for deformation banding as in the 52 kg m^{-3} sample. The divergent distributions of weak walls for the two types of foams originate from different cell wall morphologies (Fig. 7).

Previous studies showed that the roughness and damage induced by cutting degrades the stiffness and strength of the foam sample ends (Sun et al., 2016a; Meng et al., 2019). For the 75 kg m^{-3} foam, the strength distribution of cell walls is approximately uniform across the initial foam block. The degraded sample ends are thus weaker than those of the interior, which leads to first nucleation of deformation localization there. In addition, cell collapse at this layer weakens the neighboring layer which is likely to collapse sequentially to induce a spreading band. However, the sample ends are not necessariliy weaker than the interior in the heterogenous 52 kg m^{-3} sample. Deformation localization always initiates at the weakest layer across the sample, resulting in discrete deformation bands. Therefore, the spatial distribution, rather than the extent (Zaiser et al., 2013), of structural disorder plays a critical role in the nucleation of deformation bands.

5.2. Strength–density scaling law

The GA model (Gibson and Ashby, 1999) provided different scaling laws for different kinds of foams, based on their cell deformation modes. Cells of metallic foams (e.g. aluminum foam) own thick cell walls (e.g. 0.36 mm for Alporas™ (Sun et al., 2017)) and edges, and generally collapse via plastic bending of edges and stretching of walls. For conventional polymer foams (e.g. rigid PU foam, polyethylene foam), cells collapse via elastic buckling of cell edges, since cell walls are so thin (~2 μm) that the buckling resistance of walls is negligible. However, the cell wall thickness of the PMI foam is between those of the metallic foams and conventional polymer foams while its fraction of solid in walls is much higher than those of the latter two. Cell collapse in PMI foams is dominated by elastic buckling of cell walls rather than cell edges. So we propose a new strength–density relationship for PMI foams.

Appendix A shows that the bulk axial stress σ can be linearly related to the axial stress on upright walls $\sigma_{w,u}$. At the collapse point, i.e. $\sigma = \sigma_c$, a certain number of walls (including upright walls) in a layer buckle elastically and approximately simultaneously, activating the deformation banding in the foam sample. Therefore, $\sigma_{w,u}$ reaches its critical buckling strength σ_B. According to the elastic buckling theory of thin plates (Timoshenko and James, 1961), $\sigma_B \propto E_s(t_w/b_w)^2$, where E_s is the Young's modulus of wall material. Combining with Eq. (A.5), we have

$$\frac{\sigma_c}{E_s} \propto \frac{t_w^2}{b_w^2}\frac{\rho_0}{\rho_s}. \tag{9}$$

where ρ_0 and ρ_s are the initial densities of the foam and full-density material, respectively.

For a closed-cell foam, the thickness to width ratio of walls is statistically related to the relative density as (Gibson and Ashby, 1999; Wang and McDowell, 2005)

$$t_w/b_w \propto (1-\phi_0)\rho_0/\rho_s. \tag{10}$$

Substituting Eq. (10) into (9), we can express σ_c of the PMI foam as

$$\frac{\sigma_c}{E_s} \propto (1-\phi_0)^2\left(\frac{\rho_0}{\rho_s}\right)^3. \tag{11}$$

The gas-pressure contribution to the collapse strength is not considered here because it is negligible under quasi-static conditions (Sun and Li, 2015).

Voronoi modeling (Roberts and Garboczi, 2001) showed $(1-\phi_0)$ decreases with increasing relative density in a power law form, i.e. $(1-\phi_0) \propto (\rho_0/\rho_s)^{-\gamma}$. γ fitted from their simulation data is 0.62, similar to that calculated from our experimental data (0.58). Thus, Eq. (11) can be simplified as

$$\frac{\sigma_c}{E_s} = C_w\left(\frac{\rho_0}{\rho_s}\right)^{3-2\gamma}, \tag{12}$$

where C_w is a geometric constant of proportionality; the exponent is 1.84. The collapse strength of the PMI foams in our study and previous studies (Arezoo et al., 2011) are summarized in Fig. 10. The dash-dotted curve is plotted according to Eq. (12) with the best-fit $C_w = 0.049 \pm 0.001$. The experimental data agree well with the theoretical prediction.

For comparison, the collapse strength of rigid PU foams in previous studies (Calvert et al., 2010; Thirumal et al., 2010; Goods et al., 1998) are also summarized in Fig. 10, along with the theoretical strength–density relationship from the GA model.

$$\frac{\sigma_c}{E_s} = C_e\left(\frac{\rho_0}{\rho_s}\right)^2, \tag{13}$$

where C_e is a geometric constant of proportionality. The increase of collapse strength with increasing foam density is consistent with Eq. (13), with $C_e = 0.072 \pm 0.001$. In addition, the strengths of the PMI foam are considerably higher than those of the PU foam with similar densities, mainly owing to a higher modulus of matrix and a lower fraction of solid in edges.

5.3. Prediction of stress–strain curves

On the basis of the strength model (Eq. (11)), we can derive a new stress–strain relationship for the PMI foam under quasi-static uniaxial compression throughout the plastic deformation process. The axial stress σ as a function of the axial plastic strain ε_p can be expressed as

$$\frac{\sigma(\varepsilon_p)}{E_s} = C_\sigma(1-\phi(\varepsilon_p))^2\left(\frac{\rho_f(\varepsilon_p)}{\rho_s}\right)^3. \tag{14}$$

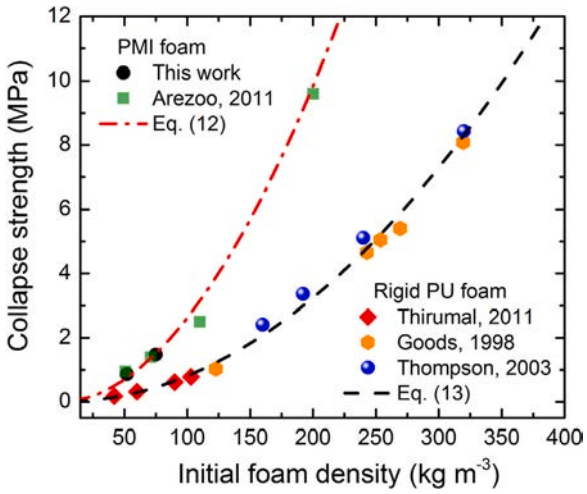

Fig. 10. Collapse strength versus initial foam density for PMI and rigid PU foams. Symbols: experimental measurements; curves: theoretical predictions.

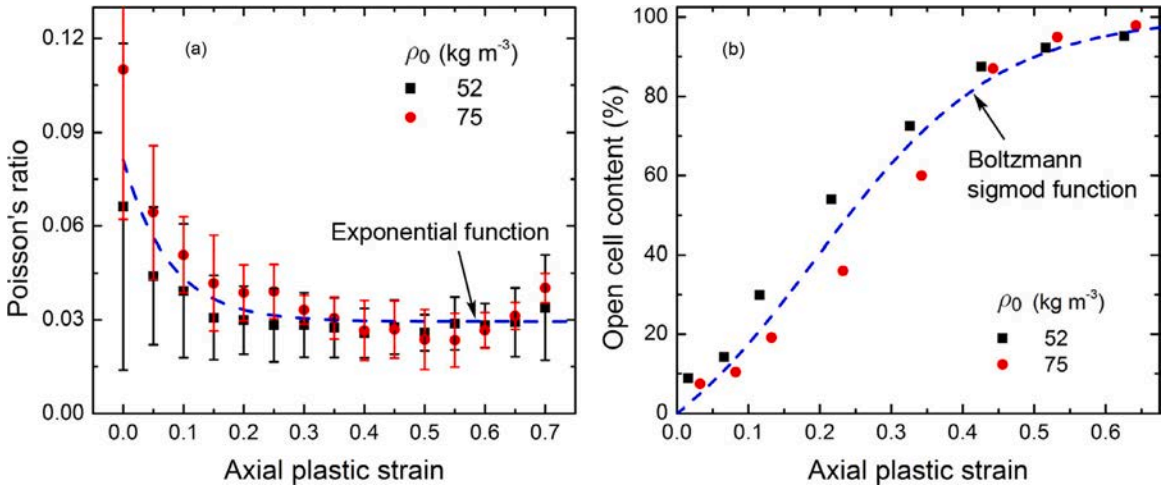

Fig. 11. Evolution of (a) the Poisson's ratio and (b) the open-cell content with the axial plastic strain for two types of foams. Symbols refer to experimental measurements, and dashed lines, fitting with the exponential (a) and the Boltzmann sigmoid function (b), respectively.

Here C_σ is a geometric constant of proportionality. $\varepsilon_p = \varepsilon - \varepsilon_c$, where ε_c is the axial strain at the collapse point. ρ_f and ϕ are the foam density and the fraction of solid in edges at the current deformation state.

ρ_f and ϕ both increase with increasing axial strain. ρ_f changes with ε_p in the following way,

$$\rho_f(\varepsilon_p) = \frac{\rho_0}{1-(1-2\nu_n)\varepsilon_p}, \tag{15}$$

where ν_n is the nominal Poisson's ratio defined as the lateral strain divided by the axial strain. ν_n quantified from three *in situ* optical imaging tests is presented in Fig. 11a. ν_n of two types of foams is similar and exhibits a similar trend. It decreases with increasing plastic strain and becomes approximately constant when the strain exceeds about 0.2. The experimental data are fitted with an exponential function,

$$\nu_n(\varepsilon_p) = \nu_{n,\infty} + A_\nu \exp\left(-\frac{\varepsilon_p}{\varepsilon_{p,0}}\right). \tag{16}$$

The fitting parameters $\nu_{n,\infty}$, A_ν and $\varepsilon_{p,0}$ are obtained to be $0.029 \pm 0.02\%$, $0.052 \pm 0.1\%$ and $7.7\% \pm 0.3\%$, respectively.

Cell collapse leads to crushing of cell walls and turns the closed-cell foam gradually into an open-cell foam. The fraction of solid in walls $1\text{-}\phi$ decreases as the volume fraction of crushed walls (f_{cw}) increases due to cell collapse. f_{cw} is defined as the volume of crushed walls normalized by the volume of total walls. f_{cw} is difficult to measure from experiments. The open-cell content f_{oc}, defined as the percentage of the volume of connected pores in the total pore volume, is calculated instead. Evolution of $f_{oc}(\varepsilon_p)$ is plotted in Fig. 11b, and is similar for two types of foams. f_{oc} is initially around zero and increases abruptly with increasing strain

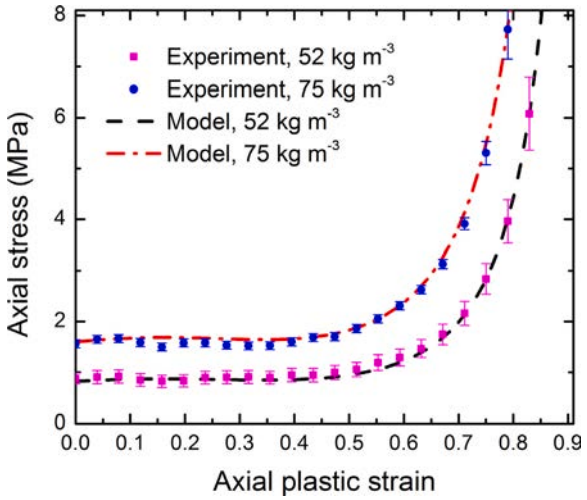

Fig. 12. Comparison between experimental stress–strain curves (solid curves) and model predictions (dashed curves).

in the collapse stage, and finally becomes stable at 100% when the sample enters the densification stage. Assume $f_{cw}(\varepsilon_p)$ is similar to $f_{oc}(\varepsilon_p)$. Therefore, $f_{oc}(\varepsilon_p)$ and $f_{cw}(\varepsilon_p)$ can be described with a Boltzmann sigmoid function,

$$f_{oc}(\varepsilon_p) \text{ or } f_{cw}(\varepsilon_p) = A_2 + \frac{-\exp(-\zeta/\eta) - A_2}{1 + \exp\left(\frac{\varepsilon_p - \zeta}{\eta}\right)}. \tag{17}$$

Here A_2 refer to the final value of f_{oc} or f_{cw}. ζ is the strain at the curve center, and η is the slope. Fig. 11b indicates $A_2 = 1$ for f_{oc}. The other parameters obtained from nonlinear fitting are $\zeta = 20.4\% \pm 2.6\%$ and $\eta = 12.5\% \pm 1.6\%$.

Therefore, $\phi(\varepsilon_p)$ is expressed as

$$\phi(\varepsilon_p) = 1 - (1 - \phi_0)\left[1 - f_{cw}(\varepsilon_p)\right] \tag{18}$$

Substituting Eqs. (15) and (18) into Eq. (14), we obtain the 1D constitutive relation for closed-cell foams under quasi-static compression as

$$\frac{\sigma(\varepsilon_p)}{E_s} = C_\sigma(1 - \phi_0)^2\left(1 - f_{cw}(\varepsilon_p)\right)^2\left[\frac{\rho_0/\rho_s}{1 - (1 - 2\nu_n(\varepsilon_p))\varepsilon_p}\right]^3. \tag{19}$$

In this model, four parameters, i.e. C_σ, A_2, ζ and η, are needed to be determined from experimental results. When $\sigma(\varepsilon_p)$ is normalized by $(1-\phi_0)^2(\rho_0/\rho_s)^3$, the stress–strain curves of foams with different initial densities coincide. The parameters obtained from nonlinear fitting are $C_\sigma = 3.40 \pm 0.01$, $A_2 = 0.75 \pm 0.04\%$, $\zeta = 20.2\% \pm 0.002$ and $\eta = 18.4\% \pm 0.05\%$. The model shows that the rate effects of PMI foams are dominated by the rate sensitivity of the elastic modulus of base polymers.

The stress–strain curves predicted by Eq. (19) are compared with the experimental curves (Fig. 12). This model reproduces well the experimental curves from collapse to densification. Compared to previous models, the fitting parameters in this model have clear physical meanings, and are independent of the initial foam density. Therefore, the model may be applied to other cellular materials where cells also collapse via elastic buckling of walls (e.g. low-density honeycombs (Cote et al., 2004; Shan et al., 2019)). In addition, although it is a volume-average model, it incorporates two microscopic effects of cell collapse, i.e. hardening via local densification, and softening via cell-wall failure. Plastic deformation of cellular materials mainly takes place in deformation bands. Local density rise in the bands leads to an increase in bulk density of the foam sample and thus a growth in bulk axial stress. However, significant cell wall crushing occurs in the bands and leads to an increase in ϕ and a decrease in the number of load-carrying members (walls), and thus a reduction in bulk axial stress. Therefore, the axial stress remains approximately constant during the collapse stage. In the densification stage, the survived walls are locked and do not crush any more, i.e. ϕ becomes approximately constant, and further increase in density due to compression leads to a monotonic stress increase.

However, deformation localization, as illustrated by DVC, is not explicitly considered in the constitutive model. It has been a challenge to integrate microscopic deformation characteristics (e.g. cell morphology, strain fields) into continuum models. Two approaches may be considered to take a step forward. The first one is statistical average or homogenization on mesoscopic behaviors of cells or its counterparts (Schraad and Harlow, 2006; Wang et al., 2018; Beckmann and Hohe, 2016). The modeling accuracy depends on the selected stochastic material representations through the use of PDFs for relevant cell parameters. These PDFs, assumed previously to be Gaussian (Schraad and Harlow, 2006) or Weibull (Wang et al., 2018), can be identified directly from *in situ* CT measurements (e.g. Eqs. (5) and (8)). The other one is the strain localization theory proposed by Rudnicki and Rice (1975). It has been widely used in deformation analyses of porous rocks and foams (Issen et al., 2005) to predict (shear or compaction) deformation

banding. Deformation banding was assumed as an instability in the constitutive description of homogeneous deformation. The strain gradient (Forest et al., 2005; Zaiser et al., 2013) can be implemented to consider the size and boundary effects critical for the foams, by introducing a characteristic length scale. The 3D strain fields from DVC, including morphology of deformation bands, may provide input database and constraints for theoretical predictions. In addition, mesoscopic FEM based on real 3D structures is a promising way of constitutive modeling of cellular materials, considering the rapid development of computation power and techniques.

6. Conclusions

Quasi-static uniaxial compression tests are conducted on the PMI foam with two initial densities, 52 kg m^{-3} and 75 kg m^{-3}. *In situ* CT is used to track the evolution of their 3D microstructures. The strain fields are mapped via DVC with the displacement and strain precision as 0.08 pixel and 0.41%, respectively. Edge segmentation is used to quantify the morphology and buckling strength indices of cell walls. Microstructure-based FE analysis is carried out to reveal buckling mechanisms of walls. The conclusions are summarized as follows:

- Multiple, discrete deformation bands is prone to form sequentially in the 52 kg m^{-3} foam sample, while spreading deformation bands prefer to initiate at sample ends and propagate across the 75 kg m^{-3} foam, as a result of divergent spatial distributions of weakest cell walls or structural heterogeneity.
- Local cell-wall buckling (marked as a gradual increase in local curvature of wall) contributes to cell collapse and thus deformation banding, which leads to about 40% reduction of cell size and reorientation of cells in the band. Collapse-induced volume shrinkage of single cells with bulk strain follows a Boltzmann sigmoid function. FE analyses verify that cell walls buckle elastically and the buckling resistance of cell walls is highly dependent on their thicknesses and inclination angles. This can be quantified with the buckling strength index. The probability distribution of the buckling strength index satisfies a lognormal distribution, and shows that the cell walls of the 75 kg m^{-3} foam sample is statistically stronger than those of the 52 kg m^{-3} foam sample, consistent with the collapse and plateau stresses. The spatial distribution of the weakest 3% walls (sorted by strength index) exhibits different characteristics for the two types of foams: concentrated in multiple discrete regions in the 52 kg m^{-3} sample while distributed nearly uniformly across the 75 kg m^{-3} sample, consistent with their macroscopic deformation modes. The spatial distribution, rather than the extent, of structural heterogeneity determines the nucleation of deformation bands.
- Based on the elastic buckling mechanism of cell walls, a new strength–density scaling law is proposed for the PMI foam and agrees well with the experimental data. Based on the strength model, an analytical constitutive model is developed to describe the plastic stress–strain curves incorporating the effects of cell collapse. The model can reproduce the stress plateau and densification stages for the two types of PMI foams, with only four fitting parameters independent of initial foam density.

Declaration of competing interest

The authors declare that they have no known competing financial interests or personal relationships that could have appeared to influence the work reported in this paper.

CRediT authorship contribution statement

H.W. Chai: Conceptualization, Methodology, Data curation. **Z.L. Xie:** Data curation. **X.H. Xiao:** Investigation. **H.L. Xie:** Investigation. **J.Y. Huang:** Conceptualization, Validation, Writing - original draft, Supervision. **S.N. Luo:** Writing - review & editing.

Acknowledgments

This work was partially supported by the National Key R&D Program of China (grant No. 2017YFB0702002), the Scientific Challenge Project of China (grant No. TZ201801), and NSFC (grant Nos. 11627901 and 11802252). This research used resources of the Advanced Photon Source, a U.S. Department of Energy (DOE) Office of Science User Facility operated for the DOE Office of Science by Argonne National Laboratory under Contract No. DE-AC02-06CH11357.

Appendix A

The axial stress distribution on a cutting plane (cross-section) perpendicular to the loading direction is inhomogeneous; the walls with lower inclination (β) angles carry smaller loads. We choose an arbitrary wall, with the longitudinal section illustrated in Fig. A.1, to derive the relationship between the axial stress on the wall and β. A displacement δh is applied to the wall, and induces compression and bending forces in it. The compression force can be calculated as

$$F_c = E_s b_w t_w \frac{\delta h}{h_w} \sin^2 \beta, \tag{A.1}$$

where E_s is the Young's modulus of wall material. t_w, b_w and h_w are the thickness, equivalent width and height of the wall. The bending force can be calculated as

$$F_b = \frac{1}{12} E_s t_w^3 b_w \frac{\delta h}{h_w^3} \sin^3 \beta \cos \beta. \tag{A.2}$$

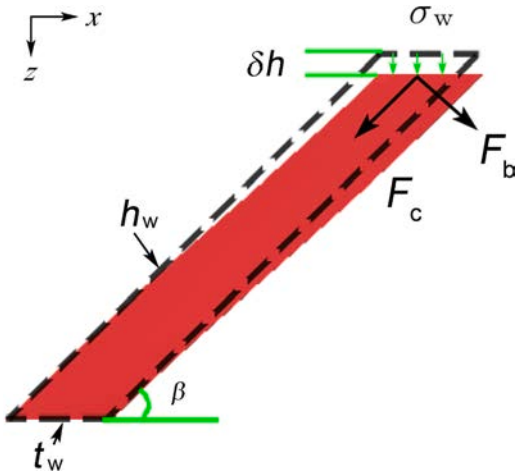

Fig. A.1. Stress analysis for an inclined cell wall of length h_w, width b_w and thickness t_w. δh: displacement applied. F_c and F_b: force components induced in the wall. β: inclination angle. σ_w: axial stress on the cross-section of the wall.

Then the axial stress on the wall σ_w is calculated as

$$\begin{aligned}\sigma_w &= \frac{F_c \sin\beta + F_b \cos\beta}{b_w t_w / \sin\beta} \\ &= E_s \frac{\delta h}{h} \sin^4\beta \left(1 + \frac{1}{12}\frac{t^2}{h^2}\cos^2\beta\right).\end{aligned} \tag{A.3}$$

For a real foam sample, the thickness to height ratio for cell walls (t_w/h_w) is less than 0.1, and the second term in the parentheses of Eq. (A.3) is negligible compared to the first term. Then, we have $\sigma_w \simeq \sigma_{w,u} \sin^4\beta$, where $\sigma_{w,u} = E_s \delta h/h$ is the axial stress on an upright wall ($\beta = 90°$). Therefore, the wall with a higher inclination angle carries a larger load.

The stress on a wall and the edges enclosing it is approximately the same considering strain continuity. The axial stress σ along the loading direction on an arbitrary cutting plane (cross-section) perpendicular to the loading direction can be calculated as

$$\sigma = \sigma_{w,u} \frac{\sum_{i=1}^{n} S_i \sin^4\beta_i}{S_f}, \tag{A.4}$$

where β_i is the inclination angle for wall i. S_i is the total area of wall i and the edges enclosing it intercepted by the cross-section. Each edge is assumed to be equally shared by the walls attached to it. n is the number of walls intercepted by this cross-section. S_f is the total cross-sectional area of the foam including the pore areas between walls.

For the cutting plane located at z_c, the summation $\sum_{i=1}^{n} S_i \sin^4\beta_i = f(z_c)S_s(z_c)$, where S_s is the total area of solid intercepted by the cutting plane. Since each cross-section contains a sufficiently large number of cells and walls with various sizes and orientations, $f(z_c)$ and $S_s(z_c)$ both vary little between different cutting planes. For a macroscopically uniform isotropic form, $S_s(z_c)/S_f \propto \rho_0/\rho_s$. Therefore,

$$\sigma \propto \sigma_{w,u} \frac{\rho_0}{\rho_s}. \tag{A.5}$$

Appendix B. Supplementary data

Supplementary material related to this article can be found online at https://doi.org/10.1016/j.ijplas.2020.102730.

References

Alkhader, M., Vural, M., 2010. A plasticity model for pressure-dependent anisotropic cellular solids. Int. J. Plast. 26 (11), 1591–1605.
Arezoo, S., Tagarielli, V.L., Petrinic, N., Reed, J.M., 2011. The mechanical response of Rohacell foams at different length scales. J. Mater. Sci. 46 (21), 6863–6870.
Arezoo, S., Tagarielli, V.L., Siviour, C.R., Petrinic, N., 2013. Compressive deformation of Rohacell foams: effects of strain rate and temperature. Int. J. Impact Eng. 51, 50–57.
Arkın, H., Janke, W., 2013. Gyration tensor based analysis of the shapes of polymer chains in an attractive spherical cage. J. Chem. Phys. 138 (5), 054904.
Avalle, M., Belingardi, G., Ibba, A., 2007. Mechanical models of cellular solids: parameters identification from experimental tests. Int. J. Impact Eng. 34 (1), 3–27.
Banda, M., Ghosh, D., 2018. Effects of porosity and strain rate on the uniaxial compressive response of ice-templated sintered macroporous alumina. Acta Mater. 149, 179–192.
Banhart, J., 2001. Manufacture, characterisation and application of cellular metals and metal foams. Prog. Mater. Sci. 46 (6), 559–632.
Bar-Kochba, E., Toyjanova, J., Andrews, E., Kim, K.-S., Franck, C., 2015. A fast iterative digital volume correlation algorithm for large deformations. Exp. Mech. 55 (1), 261–274.

Bastawros, A.F., Bart-Smith, H., Evans, A.G., 2000. Experimental analysis of deformation mechanisms in a closed-cell aluminum alloy foam. J. Mech. Phys. Solids 48 (2), 301–322.
Beckmann, C., Hohe, J., 2016. A probabilistic constitutive model for closed-cell foams. Mech. Mater. 96, 96–105.
Bie, B.X., Huang, J.Y., Fan, D., Sun, T., Fezzaa, K., Xiao, X.H., Qi, M.L., Luo, S.N., 2017. Orientation-dependent tensile deformation and damage of a T700 carbon fiber/epoxy composite: A synchrotron-based study. Carbon 121, 127–133.
Bonatti, C., Mohr, D., 2017. Large deformation response of additively-manufactured FCC metamaterials: From octet truss lattices towards continuous shell mesostructures. Int. J. Plast. 92, 122–147.
Bright, D.S., Steel, E.B., 1987. Two-dimensional top hat filter for extracting spots and spheres from digital images. J. Microsc. 146 (2), 191–200.
Calvert, K.L., Trumble, K.P., Webster, T.J., Kirkpatrick, L.A., 2010. Characterization of commercial rigid polyurethane foams used as bone analogs for implant testing. J. Mater. Sci.- Mater. Med. 21 (5), 1453–1461.
Chai, H.W., Li, H.Y., Xiao, X.H., Huang, J.Y., Luo, S.N., 2019. Correlation between cell wall buckling and deformation banding in a closed-cell foam. Scr. Mater. 170, 177–182.
Chen, Y., Das, R., Battley, M., 2017. Finite element analysis of the compressive and shear responses of structural foams using computed tomography. Compos. Struct. 159, 784–799.
Chen, R.C., Dreossi, D., Mancini, L., Menk, R., Rigon, L., Xiao, T.Q., Longo, R., 2012. PITRE: Software for phase-sensitive X-ray image processing and tomography reconstruction. J. Synchrotron Radiat. 19 (5), 836–845.
Chen, K., Scales, M., Kyriakides, S., 2019. Material response, localization and failure of an aluminum alloy under combined shear and tension: Part II analysis. Int. J. Plast. 120, 361–379.
Cote, F., Deshpande, V.S., Fleck, N.A., Evans, A.G., 2004. The out-of-plane compressive behavior of metallic honeycombs. Mater. Sci. Eng. A 380 (1–2), 272–280.
Criminisi, A., Blake, A., Rother, C., Shotton, J., Torr, P.H.S., 2007. Efficient dense stereo with occlusions for new view-synthesis by four-state dynamic programming. Int. J. Comput. Vis. 71 (1), 89–110.
Deshpande, V.S., Fleck, N.A., 2000. Isotropic constitutive models for metallic foams. J. Mech. Phys. Solids 48 (6–7), 1253–1283.
van Dijk, N.P., Wu, D., Persson, C., Isaksson, P., 2019. A global digital volume correlation algorithm based on higher-order finite elements: Implementation and evaluation. Int. J. Solids Struct. 168, 211–227.
Ehlers, W., Markert, B., 2003. A macroscopic finite strain model for cellular polymers. Int. J. Plast. 19 (7), 961–976.
Fan, Z., Zhang, B., Gao, Y., Guan, X., Xu, P., 2018. Deformation mechanisms of spherical cell porous aluminum under quasi-static compression. Scr. Mater. 142, 32–35.
Forest, S., Blazy, J.-S., Chastel, Y., Moussy, F., 2005. Continuum modeling of strain localization phenomena in metallic foams. J. Mater. Sci. 40 (22), 5903–5910.
Gibson, L.J., Ashby, M.F., 1999. Cellular Solids: Structure and Properties. Cambridge university press.
Goods, S.H., Neuschwanger, C.L., Henderson, C.C., Skala, D.M., 1998. Mechanical properties of CRETE, a polyurethane foam. J. Appl. Polym. Sci. 68 (7), 1045–1055.
Grace, I., Pilipchuk, V., Ibrahim, R., Ayorinde, E., 2012. Temperature effect on non-stationary compressive loading response of polymethacrylimide solid foam. Compos. Struct. 94 (10), 3052–3063.
Hanssen, A.G., Hopperstad, O.S., Langseth, M., Ilstad, H., 2002. Validation of constitutive models applicable to aluminium foams. Int. J. Mech. Sci. 44 (2), 359–406.
Harris, C., Stephens, M., 1988. A combined corner and edge detector. In: Alvey Vision Conference, Vol. 15. Citeseer, pp. 10–5244.
Issen, K.A., Casey, T.P., Dixon, D.M., Richards, M.C., Ingraham, J.P., 2005. Characterization and modeling of localized compaction in aluminum foam. Scr. Mater. 52 (9), 911–915.
Janik, H., Marzec, M., 2015. A review: Fabrication of porous polyurethane scaffolds. Mater. Sci. Eng. C 48, 586–591.
Kang, N.-R., Gwak, E.-J., Jeon, H., Song, E., Kim, J.-Y., 2018. Microstructural effect on time-dependent plasticity of nanoporous gold. Int. J. Plast. 109, 108–120.
Kenesei, P., Kádár, C., Rajkovits, Z., Lendvai, J., 2004. The influence of cell-size distribution on the plastic deformation in metal foams. Scr. Mater. 50 (2), 295–300.
Kim, T.-R., Shin, J.K., Goh, T.S., Kim, H.-S., Lee, J.S., Lee, C.-S., 2017. Modeling of elasto-viscoplastic behavior for polyurethane foam under various strain rates and temperatures. Compos. Struct. 180, 686–695.
Koenderink, J.J., Van Doorn, A.J., 1992. Surface shape and curvature scales. Image Vis. Comput. 10 (8), 557–564.
Lee, D.-W., Khan, K.A., Al-Rub, R.K.A., 2017. Stiffness and yield strength of architectured foams based on the Schwarz primitive triply periodic minimal surface. Int. J. Plast. 95, 1–20.
Li, H.Y., Chai, H.W., Xiao, X.H., Huang, J.Y., Luo, S.N., 2020. Fractal breakage of porous carbonate sand particles: microstructures and mechanisms. Powder Technol. 363, 112–121.
Li, Q.M., Mines, R.A.W., Birch, R.S., 2000. The crush behaviour of Rohacell-51WF structural foam. Int. J. Solids Struct. 37 (43), 6321–6341.
Liu, Q., Subhash, G., 2004. A phenomenological constitutive model for foams under large deformations. Polym. Eng. Sci. 44 (3), 463–473.
Mangipudi, K., Epler, E., Volkert, C., 2016. Topology-dependent scaling laws for the stiffness and strength of nanoporous gold. Acta Mater. 119, 115–122.
Matzke, E.B., 1946. The three-dimensional shape of bubbles in foam-an analysis of the role of surface forces in three-dimensional cell shape determination. Am. J. Bot. 58–80.
Meng, K.P., Chai, C.G., Sun, Y.L., Wang, W., Wang, Q.Y., Li, Q.M., 2019. Cutting-induced end surface effect on compressive behaviour of aluminium foams. Eur. J. Mech. A 75, 410–418.
Montminy, M.D., Tannenbaum, A.R., Macosko, C.W., 2004. The 3D structure of real polymer foams. J. Colloid Interface Sci. 280 (1), 202–211.
Naouar, N., Vidal-Salle, E., Schneider, J., Maire, E., Boisse, P., 2015. 3d composite reinforcement meso FE analyses based on X-ray computed tomography. Compos. Struct. 132, 1094–1104.
Pan, B., Wang, B., 2017. A flexible and accurate digital volume correlation method applicable to high-resolution volumetric images. Meas. Sci. Technol. 28 (10), 105007.
Patterson, B.M., Cordes, N.L., Henderson, K., Williams, J.J., Stannard, T., Singh, S.S., Ovejero, A.R., Xiao, X., Robinson, M., Chawla, N., 2016. In situ X-ray synchrotron tomographic imaging during the compression of hyper-elastic polymeric materials. J. Mater. Sci. 51 (1), 171–187.
Roberts, A.P., Garboczi, E.J., 2001. Elastic moduli of model random three-dimensional closed-cell cellular solids. Acta Mater. 49 (2), 189–197.
Roth, C.C., Morgeneyer, T.F., Cheng, Y., Helfen, L., Mohr, D., 2018. Ductile damage mechanism under shear-dominated loading: In-situ tomography experiments on dual phase steel and localization analysis. Int. J. Plast. 109, 169–192.
Rudnicki, J.W., Rice, J.R., 1975. Conditions for the localization of deformation in pressure-sensitive dilatant materials. J. Mech. Phys. Solids 23 (6), 371–394.
Rusch, K., 1970. Energy-absorbing characteristics of foamed polymers. J. Appl. Polym. Sci. 14 (6), 1433–1447.
Saadatfar, M., Mukherjee, M., Madadi, M., Schröder-Turk, G.E., Garcia-Moreno, F., Schaller, F.M., Hutzler, S., Sheppard, A.P., Banhart, J., Ramamurty, U., 2012. Structure and deformation correlation of closed-cell aluminium foam subject to uniaxial compression. Acta Mater. 60 (8), 3604–3615.
Safaei, M., Yoon, J.W., De Waele, W., 2014. Study on the definition of equivalent plastic strain under non-associated flow rule for finite element formulation. Int. J. Plast. 58, 219–238.
Schraad, M.W., Harlow, F.H., 2006. A stochastic constitutive model for disordered cellular materials: finite-strain uniaxial compression. Int. J. Solids Struct. 43 (11–12), 3542–3568.

Schrijer, F.F.J., Scarano, F., 2008. Effect of predictor–corrector filtering on the stability and spatial resolution of iterative PIV interrogation. Exp. Fluids 45 (5), 927–941.
af Segerstad, P.H., Larsson, R., Toll, S., 2008. A constitutive equation for open-cell cellular solids, including viscoplasticity, damage and deformation induced anisotropy. Int. J. Plast. 24 (5), 896–914.
Shan, J., Xu, S., Zhou, L., Wang, D., Liu, Y., Zhang, M., Wang, P., 2019. Dynamic fracture of aramid paper honeycomb subjected to impact loading. Compos. Struct. 223, 110962.
Sun, Y.L., Amirrasouli, B., Razavi, S.B., Li, Q.M., Lowe, T., Withers, P.J., 2016a. The variation in elastic modulus throughout the compression of foam materials. Acta Mater. 110, 161–174.
Sun, Y.L., Li, Q.M., 2015. Effect of entrapped gas on the dynamic compressive behaviour of cellular solids. Int. J. Solids Struct. 63, 50–67.
Sun, Y., Li, Q., 2018. Dynamic compressive behaviour of cellular materials: A review of phenomenon, mechanism and modelling. Int. J. Impact Eng. 112, 74–115.
Sun, Y.L., Li, Q.M., Lowe, T., McDonald, S.A., Withers, P.J., 2016b. Investigation of strain-rate effect on the compressive behaviour of closed-cell aluminium foam by 3D image-based modelling. Mater. Des. 89, 215–224.
Sun, Y.L., Lowe, T., McDonald, S.A., Li, Q.M., Withers, P.J., 2014. In situ investigation and image-based modelling of aluminium foam compression using micro X-Ray computed tomography. In: Visual Computing. Springer, pp. 189–197.
Sun, Y.L., Zhang, X., Shao, Z., Li, Q.M., 2017. Image-based correlation between the meso-scale structure and deformation of closed-cell foam. Mater. Sci. Eng. A 688, 27–39.
Thirumal, M., Khastgir, D., Singha, N.K., Manjunath, B.S., Naik, Y.P., 2010. Effect of foam density on the properties of water blown rigid polyurethane foam. J. Appl. Polym. Sci. 108 (3), 1810–1817.
Timoshenko, S.P., James, M.G., 1961. Theory of Elastic Stability. Dover Publications.
Wang, A.-J., McDowell, D.L., 2005. Yield surfaces of various periodic metal honeycombs at intermediate relative density. Int. J. Plast. 21 (2), 285–320.
Wang, J., Wang, H., Chen, X., Yu, Y., 2010. Experimental and numerical study of the elastic properties of PMI foams. J. Mater. Sci. 45 (10), 2688–2695.
Wang, S., Zheng, Z., Zhu, C., Ding, Y., Yu, J., 2018. Crushing and densification of rapid prototyping polylactide foam: meso-structural effect and a statistical constitutive model. Mech. Mater. 127, 65–76.
Weaire, D., Phelan, R., 1994. A counter-example to Kelvin's conjecture on minimal surfaces. Phil. Mag. Lett. 69 (2), 107–110.
Yao, Y., Chai, H.W., Li, C., Bie, B.X., Xiao, X.H., Huang, J.Y., Qi, M.L., Luo, S.N., 2018. Deformation and damage of sintered low-porosity aluminum under planar impact: microstructures and mechanisms. J. Mater. Sci. 53 (6), 4582–4597.
Zaiser, M., Mill, F., Konstantinidis, A., Aifantis, K.E., 2013. Strain localization and strain propagation in collapsible solid foams. Mater. Sci. Eng. A 567 (4), 38–45.
Zaretsky, E., Asaf, Z., Ran, E., Aizik, F., 2012. Impact response of high density flexible polyurethane foam. Int. J. Impact Eng. 39 (1), 1–7.
Zheng, Z., Wang, C., Yu, J., Reid, S.R., Harrigan, J.J., 2014. Dynamic stress–strain states for metal foams using a 3D cellular model. J. Mech. Phys. Solids 72, 93–114.